Quaternary Geochronology 73 (2022) 101373

Contents lists available at ScienceDirect

Quaternary Geochronology

journal homepage: www.elsevier.com/locate/quageo

Dating of megaflood deposits in the Russian Altai using rock surface luminescence

Daria V. Semikolennykh [a,*], Alastair C. Cunningham [b,c], Redzhep N. Kurbanov [d], Andrei V. Panin [e], Ivan D. Zolnikov [f], Evgeny V. Deev [g], Andrew S. Murray [h]

[a] Dovzhenko str., 12/1, 14, 119285, Moscow, Russia
[b] DTU Physics, Technical University of Denmark, Risø Campus, DK, 4000, Roskilde, Denmark
[c] Department of Geography, Royal Holloway, University of London, Egham, UK
[d] Profsoyuznaya str., 104, 517, 117437, Moscow, Russia
[e] Orshanskaya str., 9, 258, 121359, Moscow, Russia
[f] Morskoy ave., 40, 24, 630090, Novosibirsk, Russia
[g] Ekvatornaya str., 15, 77, 630060, Novosibirsk, Russia
[h] Department of Geoscience, Aarhus University, Risø Campus, DK, 4000, Roskilde, Denmark

ARTICLE INFO

Keywords:
Rock surface dating
Russian Altai
Megaflood deposits
Palaeoearthquake
Pleistocene
Holocene

ABSTRACT

Catastrophic drainage of ice-dammed lakes in the Altai Mountains has been inferred from geomorphological evidence in the Katun Valley (Russia), and is presumed to have occurred during the Pleistocene. The sedimentary features have been difficult to date directly, due to the absence of organic carbon, and the improbability that luminescence signals in sand grains would be reset during transport. However, the development of rock-surface luminescence dating provides a new opportunity to date the features: clasts have a different transport history to sand grains, and their luminescence depth profiles can be inspected for evidence of bleaching before burial. Here we investigate two sites in the Altai Mountains, and use rock-surface luminescence burial dating to constrain the age of the megaflood deposits. In the Katun Valley, we sampled granite cobbles from a frozen sediment clast emplaced as a dropstone within a massive megaflood gravel terrace. Burial ages for the clasts range from 16.7 to 21.4 ka, with a mean age of 19.8 ± 1.5 ka. This represents the depositional age of the fluvial sediments that preceded the lake outburst flood, (and hence places a maximum age on the catastrophic flood). Clasts sampled from mega-ripples in the Kurai Basin are shown to have a mid-to-late Holocene burial age, which is not consistent with the possible origin of these features during a catastrophic drainage of a glacier-dammed lake. Instead, the burial age of the Kurai Basin sediments may reflect local-scale periglacial or seismic processes along the Kurai Fault Zone.

1. Introduction

The Russian Altai contains a number of unusual geomorphological features, interpreted since the 1970’s as evidence of catastrophic discharge of ice-dammed lakes of the Altai Mountains (e.g. Baryshnikov, 1979; Butvilovsky, 1982; Rudoy, 1984). These flood deposits gained prominence in the 1990s through the work of international researchers (Baker et al., 1993; Carling et al., 2002; Herget, 2005). The primary evidence is located in the valley of the Katun River, its tributary the Chuya River, and at the bottom of the Kurai Depression. This evidence includes long-wavelength gravel dunes, spillways, vehicle-sized blocks of rock clearly transported over considerable distances (hundreds of kilometers), and up to 200-m-thick gravel deposits apparently made up of a single unit. Each of these features is evidence of the enormous scale of the flood(s) responsible. Baker et al. (1993) ranked the Altaian outburst flood as one of the five most powerful fluvial disasters in the history of the Earth.

A range of radiogenic dating methods (cosmogenic ^{10}Be, ^{14}C, Thermoluminescence, Optically Stimulated Luminescence (OSL)) have provided dates in the range 12–26 ka for megaflood-related sediments. These include: deposits in glacier- and moraine-dammed lakes in the Kurai Basin and surroundings; large blocks on the surfaces of post-megaflood terraces in the Katun Valley and in the bottom of the Kurai Basin; and loess overlying megaflood deposit (Lehmkuhl et al., 2007;

---

* Corresponding author. Dvzhenko str., 12/1, 14, 119285, Moscow, Russia.
E-mail address: aristova@igras.ru (D.V. Semikolennykh).

https://doi.org/10.1016/j.quageo.2022.101373
Received 15 June 2022; Accepted 21 July 2022

Reuther et al., 2006; Panin et al., 2015c; Zolnikov et al., 2016; Deev et al., 2019; Agatova et al., 2020; Herget et al., 2020). However, ^{14}C and OSL dates for features in the Chuya and Katun valleys, their tributaries, and in the Uimon Basin, indicate ages in the range of 40–100 ka. The features dated at these locations include deposits of glacier-dammed lakes; glaciofluvial and alluvial deposits; and loess stratigraphically overlying the megaflood strata (Panin et al., 2015a, b, 2021; Zolnikov et al., 2016; Deev et al., 2019). Some authors have thus suggested that the catastrophic breakthrough of dammed lakes in the Russian Altai, and in particular in the valleys of the Katun and Chuya rivers, took place more than once (Butvilovsky, 1993; Carling et al., 2002; Zolnikov, 2008; Zolnikov and Deev, 2013; Zolnikov et al., 2016; Deev et al., 2019). However, there is still no consensus regarding the number of catastrophic breakthroughs in the Pleistocene history of these valleys, or on their qualitative and quantitative characteristics.

The main problem in the study of megaflood deposits in the Russian Altai is the lack of reliable geochronological data obtained directly from these deposits. The absence of organic material in the sediment precludes the use of the radiocarbon dating. Conventional luminescence dating methods can result in overestimated ages, because the sediment was transported rapidly over short distances, reducing the likelihood that the material was sufficiently light exposed before burial.

Over the last 10 years a new application of luminescence dating – rock surface burial dating – has been developed (Sohbati et al., 2011, 2012a; Sohbati et al., 2015; Freiesleben et al., 2015). As with sand grains, the luminescence signals of rock surfaces are reset through light exposure, and signals re-accumulate during burial through the absorption of ionizing radiation. When applied to buried cobbles or boulders, the method provides an alternative means of dating sediment – such as catastrophic flood deposits – where dating of sand grains may not be possible. Large clasts have a different transport history to finer sediment, and some clasts are likely to have had prolonged daylight exposure prior to final transport and deposition (e.g Rades et al., 2018; Cunningham et al., 2022). In the Altai, thick terraces and giant ripples created by the catastrophic flood include occasional beds of cobbles and boulders. By targeting these clasts for rock-surface burial dating, there is potential to

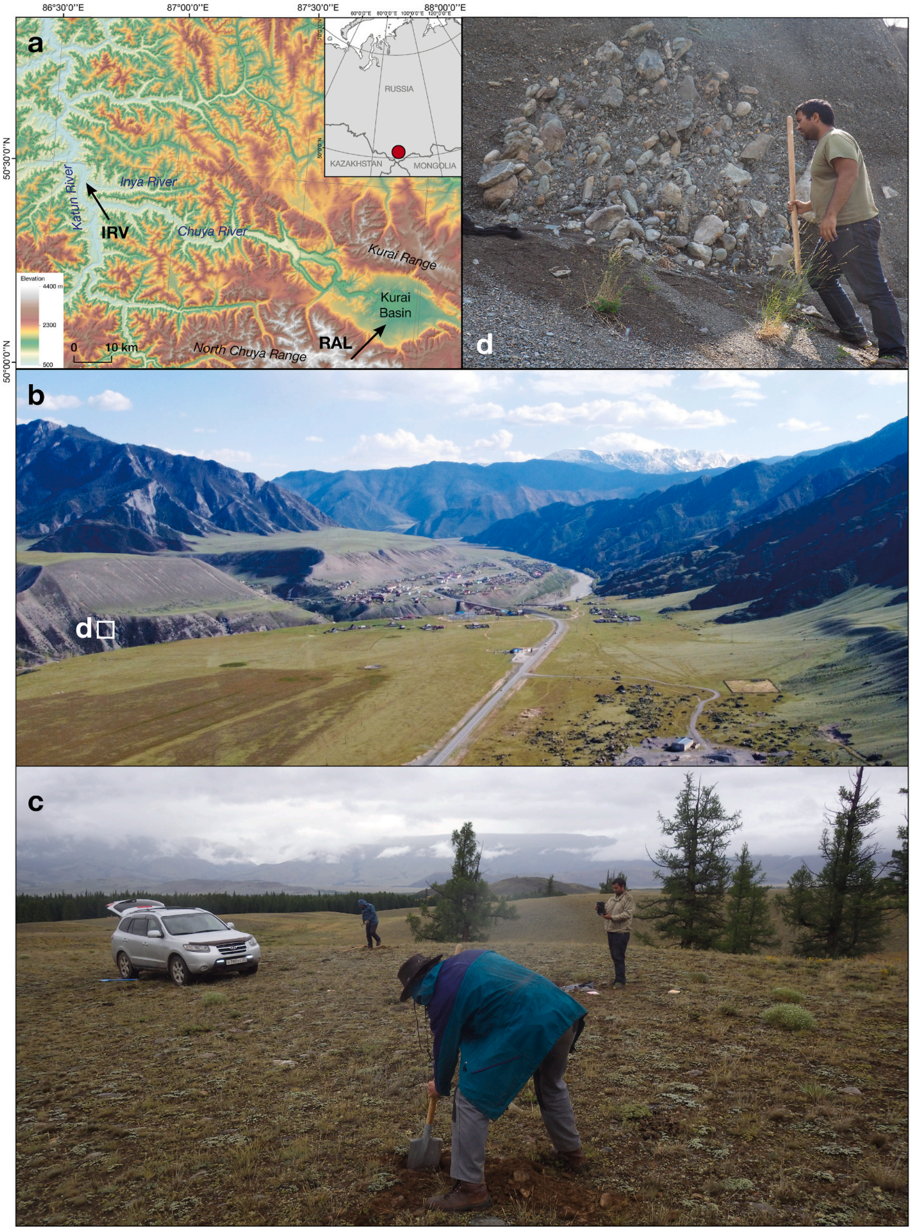

Fig. 1. The location of the sampling sites in Russian Altai, inset shows the study area in west Siberia; b) location of the IRV site in the Katun River terrace; c) sampling site RAL on the top of the giant ripple; d) Frozen sediment dropstone IRV.

obtain new age constraints on the flood sediment. Furthermore, by measuring the way in which the luminescence signal increases with depth into the rock surface, it is possible to determine on a clast-by-clast basis whether the grains at the surface were fully bleached prior to deposition, and to assess the degree of fading of the luminescence signal.

The Russian Altai is also subject to another type of catastrophic process – earthquakes – and these are potentially implicated in the build-up or initiation of megafloods. The last large Chuya earthquake (Ms = 7.3) occurred at the southern borders of the Kurai and Chuya basins on September 27, 2003. Large palaeoearthquakes are also characteristic of the Late Pleistocene–Holocene history of the Russian Altai (Deev et al., 2009, 2013, 2018; Deev, 2019; Turova et al., 2020). These palaeo events not only leave surface ruptures, but have also formed large landslides and rockfalls, which, along with glacial dams, likely contributed to the formation of dammed lakes in the Chuya and Katun River valleys. Our study sites (Fig. 1a) are located on the Katun active fault line (Deev et al., 2005, 2012, 2015, 2019) drained by the river Katun, or in the immediate vicinity of the Kurai and North Chuya fault zones, bordering the Kurai Basin from the north and south respectively (Deev et al., 2017; Turova et al., 2020).

In this paper we set out to test the application of rock-surface burial dating to large clasts moved by megafloods in the Altai, and to obtain new radiometric age constraints on two of the major flood features in the region. The first site is a massive gravel deposit on the Katun River; the second site is the inferred lake source region, Kurai Basin, where giant surface ripples are visible over almost the entire area.

2. Material and methods

2.1. Samples from the Katun River terrace and the Kurai Basin

Cobbles were sampled during fieldwork in July 2018. The first series (IRV) of samples was taken from an outcrop of a fluvial terrace (50°27′49.6″N 86°38′18.3″E) of the Katun River 300 m below the confluence of the Inya River (Fig. 1b). Here megaflood parallel and cross-bedded sandy gravel, pebble and cross-bedded boulder-block deposits are exposed, the latter being mainly confined to the lower part of the section.

The sampling was carried out from a previously frozen accumulation of cobbles and finer sediment making up a single 2 × 2.5 m large dropstone that stands out against the background of the finer deposits of the terrace (Fig. 1d). The presence of dropstones of different sizes is a hallmark of megaflood deposits. They represent displaced blocks of frozen alluvial deposits, or deposits of previous megafloods (Carling, 2013; Zolnikov and Deev, 2013). Several granite clasts were sampled from this alluvial dropstone. Their exposed surface was spray-painted for identification, and the clasts were wrapped in aluminium foil as they were removed from the surrounding sediment. After unpacking the samples under red light in the laboratory all clasts could be identified as light medium-grained granites (IRV 13, 15). The clasts are well-rounded, roughly 15–20 cm in diameter.

The second series of samples (RAL) was collected from the giant ripples (Fig. 1c) in the Kurai Depression (50°10′23.9″N 87°55′23.4″E) – the presumed bed of the formerly ice-dammed lake. In plan, the giant ripples represent a system of elongated, slightly meandering ridges oriented sub-perpendicularly to the current strike of the valleys, up to 20 m high (Rudoy, 1995). The ridges consist of well-sorted pebble-to-small-boulder deposits with a limited amount (no more than 10%) of coarse-grained sands. Buried clasts were taken from immediately below the surfaces of the mega ripples. The clasts were cobble-sized and well rounded. After unpacking the samples under red light in the laboratory one cobble could be identified as light medium-grained granite (RAL 1830), another (RAL 1833) as quartzite. Additional sediment samples were collected from each site to aid in gamma dose rate determination.

2.2. Sample preparation

Initial sample preparation was conducted at the Research Laboratory of Recent Sediments and Pleistocene Palaeogeography at Lomonosov Moscow State University (Russia), and luminescence measurements were performed at the Nordic Laboratory for Luminescence Dating (Aarhus University and Technical University of Denmark, Denmark). Cores were drilled from each buried clast surface using a water-cooled diamond-tipped drill (Optimum maschinen OPTI B 17 Pro). Diameters of all cores are ~10 mm with various lengths of up to ~25 mm. The cores were sliced at known 1.5 mm increments with a water-cooled low-speed diamond wafering saw (SYJ-150 Digital Low Speed Diamond Saw, MTI corporation) to produce slices of thickness ~1.2 mm. Further material from each clast was collected for gamma spectrometry.

3. Luminescence measurements

3.1. Depth profiles and equivalent dose

Luminescence measurements were carried out on several Risø TL/OSL readers, Model TL-DA15. Beta irradiation used a calibrated ^{90}Sr/^{90}Y beta source, luminescence signals were stimulated using infra-red (850 ± 30 nm) LEDs and detected by photo-multiplier with detection optics comprised of Schott BG-39 (2 mm thickness) and Corning 7–59 glass (4 mm thickness) filters.

Luminescence depth profiles were measured using a post-IR protocol (Thomsen et al., 2008; Buylaert et al., 2009) according thesingle-aliquot regenerative-dose procedure (SAR; Murray and Wintle, 2000, Table 1). Two IR stimulations – one at 50 °C (IR$_{50}$), and subsequent one at 225 °C (pIRIR$_{225}$) – provide two luminescence signals with which to assess the degree of bleaching within the clast. A high temperature IR stimulation at 260 °C at the end of each cycle was employed to minimise possible signal transfer to the next cycle (Murray and Wintle, 2003). Slices were measured directly in the sample carousel of the reader.

Equivalent doses have been estimated using one of two methods, depending on the quantity of material available from the clasts. For IRV-13 and15, depth profiles for the chosen face have been fitted with a bleaching model (Freiesleben et al., 2015) to ascertain whether the surface slices were sufficiently bleached before burial. Further short cores from the same clast face were available for separate equivalent

Table 1
The SAR protocols used in this study. (a) IR50 protocol for D_e, used for samples IRV-13 and 15. (b) A post-IR protocol used for profile measurements, and D_e estimation for the Kurai Basin samples.

Step	Treatment (a)	Observed (a)	Step	Treatment (b)	Observed (b)
1	Preheat 250 °C for 210s		1	Preheat 270 °C for 210s	
2	Stimulation with IR for 210s at 50 °C	Lx (IR$_{50}$)	2	Stimulation with IR for 210s at 50 °C	Lx (IR$_{50}$)
			3	Stimulation with pIR IRSL for 210s at 225 °C	Lx (pIRIR$_{225}$)
3	Test dose		4	Test dose	
4	Preheat 250 °C for 210s		5	Preheat 270 °C for 210s	
5	Stimulation with IR for 210s at 50 °C	Tx (IR$_{50}$)	6	Stimulation with IR for 210s at 50 °C	Tx (IR$_{50}$)
			7	Stimulation with pIR IRSL for 210s at 225 °C	Tx (pIRIR$_{225}$)
6	Stimulation with IR for 210s at 260 °C		8	Stimulation with IR for 210s at 260 °C	
7	Dose		9	Dose	

dose measurements, mirroring the procedures previously used (e.g. Freiesleben et al., 2015; Jenkins et al., 2018; Souza et al., 2019; Ageby et al., 2021; etc.). D_e for the surface and near-surface slices was estimated using the IRSL signal at 50 °C, within a standard single aliquot regenerative dose protocol for feldspar (Wallinga et al., 2000, Table 1). Dose-response curves (Fig. 2A-B) were fitted in R v. 4.0.3 with the *plot_GrowthCurve* function from the *Luminescence* package (Kreutzer and Dietze, 2021). For the IRV samples, single cores were obtained for additional faces of each clast; these were profiled using the post-IR measurement, so providing an IR_{50} and a $pIRIR_{225}$ signal. To estimate D_e for these surfaces, the dose response of the outer slices was defined using the post-IR SAR protocol (Buylaert et al., 2009). Profiles were fitted using a simplified bleaching model and the inferred burial signal projected onto the dose-response curve (Cunningham et al., 2022). This procedure allows D_e to be estimated from very limited quantities of material and – in principle – to estimate burial doses for cores that have not been fully bleached. The disadvantage of its application, in this case, is that the D_e is obtained using the IR_{50} signal from within the post-IR protocol, which is less accurate when judged by dose recovery tests. This procedure is also applied to the two clasts from the Kurai Basin ripple deposits.

Dose recovery tests were performed on 2–3 slices per sample using the IR_{50} protocol. Slices were taken from the innermost part of cores where the natural signal can be expected to be in saturation, bleached for >24 h in a solar simulator (Hönle SOL 2), and given a beta dose of ~35 Gy. Doses were then estimated to assess the ability of the protocol to recover the given dose. Dose-recovery ratios range between 0.86 and 1.17; the mean across all samples is 1.00 ± 0.03, and overdispersion 7.5% (Fig. 3). For the second method of D_e estimation used here, in which the IR_{50} signal is obtained from a post-IR protocol, dose recovery results tend to be less accurate; nevertheless, the burial doses obtained have been found to be consistent between different signals used, and are reproducible between clasts (see Cunningham et al., 2022).

3.2. *Fading*

Depth profiles were exploited for fading correction. The deepest slices in most cores can be assumed to have a signal in field saturation; this is the condition in which the rate of signal fading is equal to the radiation-induced signal accumulation. Following profile measurements, the innermost slices were given a very large dose (~1800 Gy) and re-measured. The ratio of the natural saturation level to the laboratory induced saturation level gives an estimate of the degree of fading during the burial period. This method of fading correction is only possible where field saturation is obtainable, and has been used successfully a number of times (e.g. Rades et al., 2018; Cunningham et al., 2021).

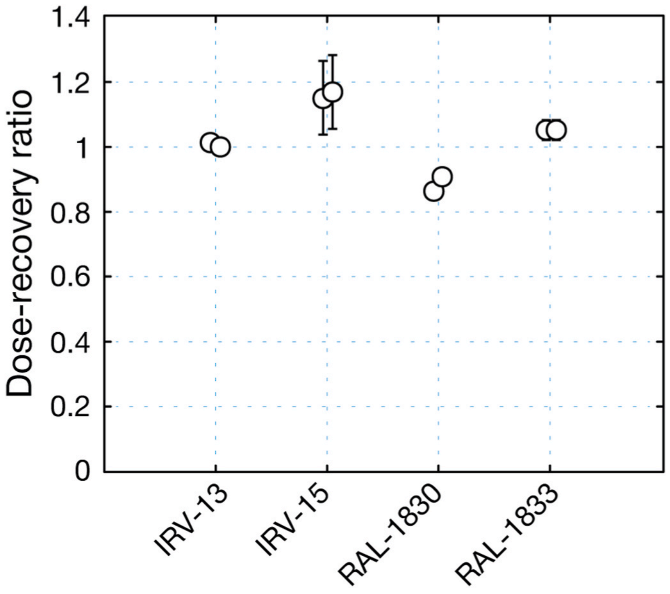

Fig. 3. Dose-recovery results for each sample using the IR_{50} protocol, showing two slices for each sample. The average ratio over the four samples is 1.00 ± 0.03, and overdispersion is 7.5%.

3.3. *Dose rate*

The radionuclide concentrations (^{226}Ra, ^{232}Th and ^{40}K) in the boulders and in the surrounding sediment were measured with a high-purity germanium detector for ~24 h, following the procedures of Murray et al. (1987, 2018). All samples were first pulverized and homogenized. Sediment samples were ignited at 450 °C for 24 h to remove organic material. The homogenized material was cast in wax in a disc- (rocks) and a cup-shaped (sediments) mould and left for >3 weeks to achieve ^{222}Rn equilibrium. Results of the measurements are presented in Table 2. Dry infinite-matrix dose rates were calculated using the conversion factors of Cresswell et al. (2018). Beta attenuation due to grain size followed Cunningham et al. (2021), assuming a homogenous distribution of radionuclides within grains. The effective grain size for beta attenuation calculations, and the internal ^{40}K dose rate, was estimated using micro-XRF measurements on a selection of slices: the spatial distribution of K for five slices from each clast (Fig. 4) was measured using a Bruker M4 Tornado micro-XRF spectrometer. This data was used to estimate the average feldspar grain size in our samples. Following Rades et al. (2018) we used the graphical software ImageJ to convert the possible grains seen in the μ-XRF element mapping into ellipsoids and take the mean ferrets to represent grain size range (Table 3).

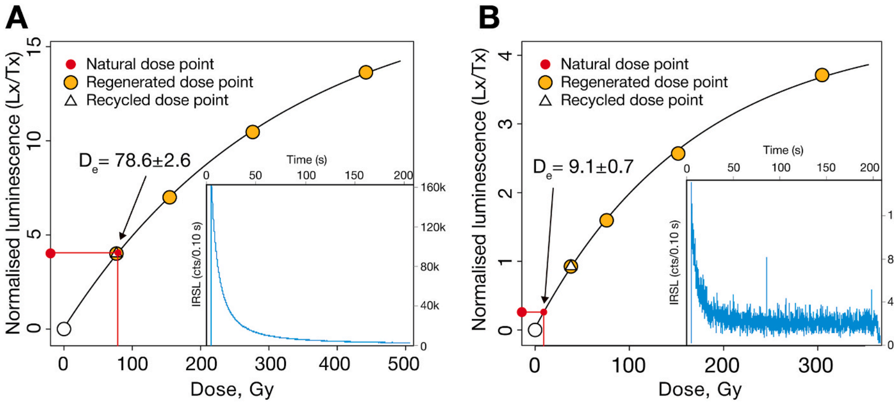

Fig. 2. Representative dose response curves for (A) IRV13 (granite) at ~1.5 mm depth from the top surface, and (B) RAL1833 (quartzite) at ~4.5 mm depth from the bottom surface. The insets show the natural $IRSL_{50}$ decay curve for the same slices.

Table 2

Dose rate data for clasts and sediment. Radionuclide activity concentrations measured using HpGe Gamma spectrometry. Total dose rates include contributions from alpha, beta, gamma and cosmic components; grain-size corrections have been applied to the beta dose. Gamma dose rates take account of both clast and sediment contributions.

Sample no	Sample type	^{226}Ra (Bq kg^{-1})	^{232}Th (Bq kg^{-1})	^{40}K (Bq kg^{-1})	Mean grain size (µm)	Dose rate (Gy ka^{-1})
IRV 13	Cobble	19.4 ± 10.5	45.0 ± 0.9	1230.4 ± 24.5	385	5.93 ± 0.24
IRV 15	Cobble	24.6 ± 5.7	101.9 ± 1.1	887.7 ± 17.5	303	4.76 ± 0.20
RAL 1830	Cobble	47.6 ± 1.0	118.8 ± 1.3	250.8 ± 13.0	254	4.69 ± 0.17
RAL 1833	Cobble	22.4 ± 0.4	21.5 ± 0.4	78.4 ± 4.0	137	1.76 ± 0.09
IRV	Sediments	24.0 ± 0.5	20.8 ± 0.6	468.0 ± 0.9		2.4 ± 0.1
RAL 1830	Sediments	31.9 ± 0.6	29.8 ± 0.7	737.0 ± 12.0		3.6 ± 0.1
RAL 1833	Sediments	5.3 ± 0.4	3.3 ± 0.3	333.0 ± 10.0		0.8 ± 0.1

Further corrections were made to the gamma and beta dose rates to account for geometrical non-homogeneity. The estimated gamma dose rates make use of the clast and sediment activity concentrations, assuming 50% dose weighting from each, and assigning a 25% uncertainty to the 'sediment' portion of the gamma dose rate. This extra uncertainty reflects our lack of knowledge of the true gamma dose rate derived from (unsampled) clasts buried close to the sampled clast (see Fig. 1d). For the beta dose rate, a 50% clast/sediment weighting is applied to the surface slice only. For all other slices (from a depth of 1.5 mm onwards), the beta dose rate comes entirely from the clast. These are crude assumptions based on the approximate ranges of beta and gamma radiation in rock (see Aitken (1985), appendix H); but in the case of the beta range is also consistent with the Monte Carlo results of Riedesel and Autzen (2020). We note that more precise dose weightings can be obtained from Monte Carlo modelling (e.g. Riedesel and Autzen, 2020), but do not consider such an approach worthwhile given the uncertainty in the geometry described above. Water content within clasts is negligible and has been omitted from the dose rate calculations. A small internal alpha dose rate of 0.06 ± 0.03 Gy ka^{-1} to feldspar grains has been assumed. Cosmic dose rates have been included for the (near-surface) Kurai Basin clasts, with calculations following Prescott and Hutton (1994).

4. Results

4.1. Site 1: Katun terrace

Two clasts from the dropstone sediment provided bleaching profiles. Clast IRV-13 shows a bleaching profile on two faces. For the first core, a burial dose plateau is evident at a depth of 1.5–4.5 mm. However, the surface slice returns a slightly lower signal (Fig. 5a). Further short cores were extracted from this face, and used to define the dose (Fig. 5b). These short cores also display a diminished signal for the surface slice. For this clast, the external beta dose rate is slightly lower than the clast's beta dose rate, but not by enough to explain the low signal for the surface slices. It is more likely that this surface of the clast received a recent, short period of bleaching, most likely reflecting an exposed surface immediately before sampling. This is supported from the second profile from the same clast (from a different face), which has no unusual depletion of the surface signal. By omitting the surface slice from the short cores, the estimated D_e from is 86.9 ± 4.8 Gy (IR$_{50}$, uncorrected for fading). The profile from a second core - from a different face - can also be converted into a dose estimate, by projecting the fitted L_n/T_n onto the

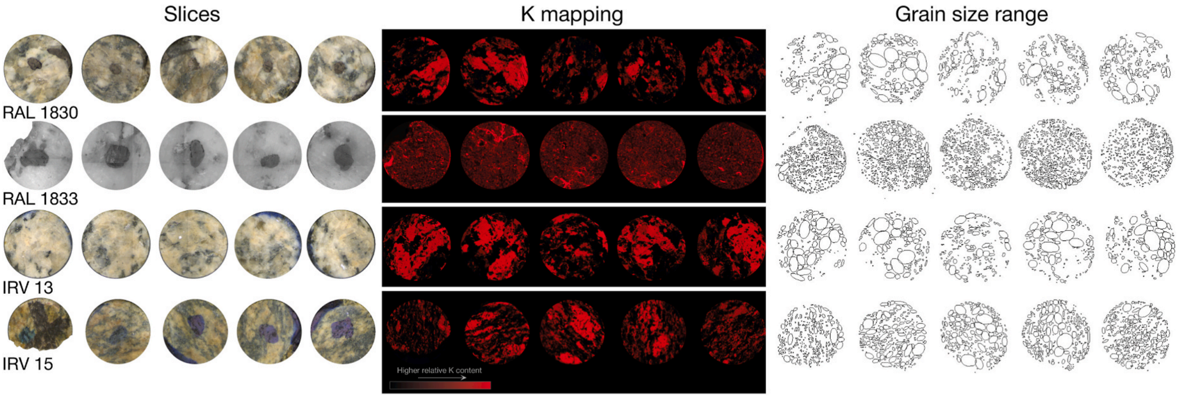

Fig. 4. Lithologies collected from IRV and RAL sites. The relative potassium concentrations within the slices were mapped with µXRF and convert into ellipsoids. The slices are ∽10 mm in diameter.

Table 3

Estimated burial ages for all clasts. All D_e measurements use the IR$_{50}$ signal unless stated otherwise. Some clasts have multiple age estimates, resulting from the different cores or methods used: Fractions labelled 'profile fit' have had D_e evaluated by fitting of the depth profile. Otherwise, D_e has been estimated by multiple slices from additional short cores. (*) indicates assumed values, see text for justification.

Clast	Fraction	Uncorrected D$_e$ (Gy)	Sat. Ratio	Corrected D$_e$ (Gy)	Aga (ka)
IRV 13	Slices 1.5–3 mm	86.9 ± 4.8	0.82 ± 0.03	106.0 ± 7.0	17.7 ± 1.5
	Core B: profile fit	105.3 ± 4.9		128.3 ± 7.6	21.4 ± 1.7
IRV 15	Surface slices	56.2 ± 4.7	0.70 ± 0.03	80.5 ± 7.6	16.7 ± 1.8
	Slices 1.5 mm	82.9 ± 5.7		118.7 ± 9.6	21.4 ± 2.0
	Core B: profile fit	63.9 ± 3.7		91.5 ± 6.6	19.0 ± 1.7
	Core C: projected	72.2 ± 3.8		103.4 ± 7.0	21.4 ± 1.8
RAL 1830	Core A: profile fit	7.3 ± 0.3	0.93 ± 0.06	7.8 ± 0.6	1.7 ± 0.1
	Core A: profile fit (pIR-225)	10.1 ± 0.6	0.97 ± 0.03*	10.4 ± 0.7	2.2 ± 0.2
RAL 1833	Core A: projected	9.0 ± 0.5	0.80 ± 0.20*	11.2 ± 2.9	6.4 ± 1.7

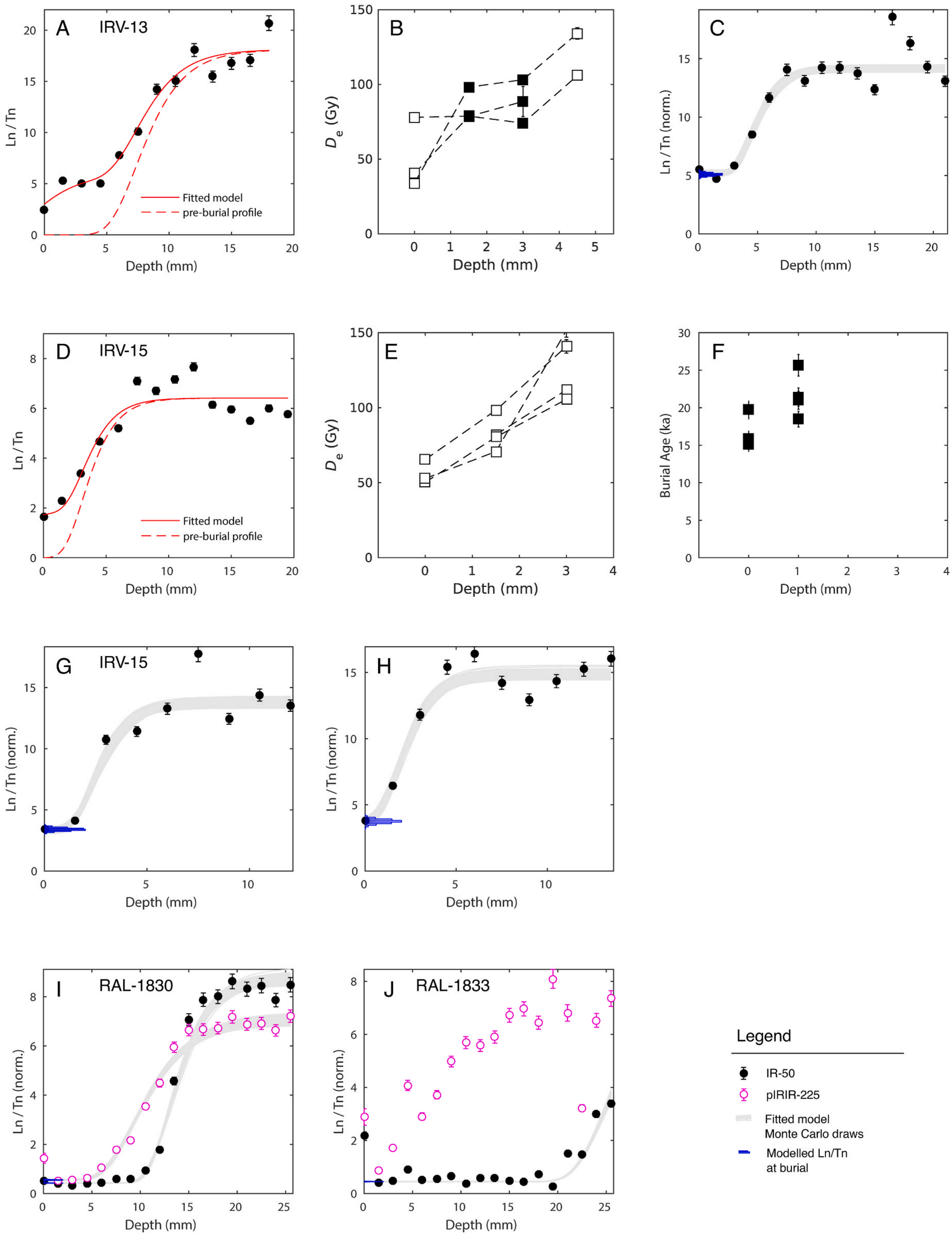

Fig. 5. Luminescence depth profiles for the clasts in this study: **IRV-13**: (a) Luminescence depth profile of IRV-13, face A, fitted with a double bleaching and burial model. Also shown is the inferred depth of bleaching before burial. (b) Measured D_e for three short cores taken from face A of IRV-13 (uncorrected IR$_{50}$); filled symbols slices used for D_e estimation. (c) Further profile from face B, fitted with a one-bleach, one-burial model. **IRV-15**: (d). Luminescence depth profile of IRV-13, face A, fitted with a double bleaching and burial model. (e) D_e from three further short cores from face A, plotted against depth (uncorrected IR$_{50}$). (f) Burial ages implied by the first two slices of each short core. The effect of a low external beta dose rate has been applied to the surface slices. (g) and (h) luminescence profiles for cores taken from two other faces of the clast, fitted with a 1-bleach 1-burial model. **RAL-1830**: (i) IR$_{50}$ and pIR$_{225}$ depth profiles from a single core of RAL-1830, fitted with a 1-bleach-1-burial model. **RAL-1833**: (j) IR$_{50}$ and pIR$_{225}$ depth profiles from a single core of RAL-1833, fitted with a 1-bleach-1-burial model for IR$_{50}$ only.

dose response curve. This provides a second estimate of D_e of 105.3 ± 4.9 Gy (IR_{50}, uncorrected). Using the measured saturation ratio of 0.82 ± 0.03, two estimates of clast burial age can be defined: 17.7 ± 1.5 ka, and 21.4 ± 1.7 ka for face A and face B, respectively, with a mean of 19.6 ± 1.5 ka.

Three profiles have been measured for clast IRV-15. The first has been fitted with a bleaching model, indicating the surface slice was sufficiently bleached before burial (Fig. 5d) and giving a saturation ratio of 0.70 ± 0.03 for the IR_{50} signal. The equivalent dose has been measured for three slices from each of three short cores taken from the same face of the clast (Fig. 5e); their implied burial ages are also shown (Fig. 5f). Further burial profiles were obtained from different faces of the clast (Fig. 5g–h); which are used to provide separate estimates of D_e. Age estimates for the clast range from 16.7 to 21.4 ka, with an average of 19.6 ± 1.5 ka.

4.2. Site 2: Kurai Basin

Two clasts from the Kurai Basin mega-ripples provide very good bleaching profiles. RAL-1830 is a granite cobble, showing bleaching in both the IR_{50} and pIR_{225} signal (Fig. 5i). Signal saturation is reached after 15 mm depth, allowing a saturation ratio to be measured (0.93 ± 0.06 for IR_{50}). A measurement error prevented the pIR_{225} saturation ratio from being defined; however, it is constrained (in principle) to lie between that of the IR_{50} and unity, so we assume a value of 0.97 ± 0.03. In the absence of short cores, the fitted surface Ln/Tn has been used to estimate the burial dose and age from each signal (Table 3); clast burial age is estimated as either 1.7 ± 0.1 ka (IR_{50} signal) or 2.2 ± 0.2 ka ($pIRIR_{225}$).

Clast RAL-1833 is a quartzite cobble, also displaying an extensive bleaching profile (Fig. 5j) in the IR_{50} signal, but limited bleaching of the pIR_{225} signal. Due to the depth of bleaching, no slice indicates the field saturation signal, and so the saturation ratio could not be measured. For age estimates, we assume a ratio of 0.80 ± 0.20. This range covers the likely observed saturation ratios for the IR_{50} signal measured in this study and elsewhere, and allows an imprecise age to be calculated. The burial age is estimated from the IR_{50} signal as 6.4 ± 1.7 ka.

5. Discussion

Luminescence profiles obtained from cobbles from two locations showed that these samples were exposed to sunlight prior to burial. Two groups of dates can be distinguished, corresponding to two distinct events. Clasts from the sediment-dropstone in the Katun terrace indicate a burial age in the range of 16.7 and 21.4 ka, with a central estimate of 19.6 ± 1.5 ka. This age reflects the last episode of bleaching for the clasts, which is likely to be the time of their deposition in their original fluvial setting. Their transport as a frozen sediment unit, and deposition in the gravel terrace, must post-date this bleaching event. The burial age of 16.7–21.4 ka is therefore a maximum age estimate for the catastrophic flood that emplaced the dropstone in the Katun terrace.

Four lakes can be considered as a source of water for a major flood event in this age interval. The first of them – Baratalskoe – arose as a result of damming the Chuya River Valley by the Maashey glacier in MIS-2; this glacier spread into the Kurai Depression (Agatova et al., 2020; Zolnikov et al., 2021). The degradation of glaciers and the draining of the dammed lake dates back to 18–19 ka years ago, but the very catastrophic nature of this drainage remains controversial (Panin et al., 2015c; Gribenski et al., 2016; Agatova et al., 2020; Herget et al., 2020). The Chuya Valley and partly the Chuya Depression were also dammed by a large seismogenic landslide in the 10–16 ka BP period (Zolnikov et al., 2021; Deev et al., in press), but this drainage was not catastrophic. In the Uimon Basin about 14–20 ka BP, there was also landslide-dammed lake, which drained during the destruction of the dam, flooding the Katun Valley (Deev et al., 2018). Finally, directly in the Katun Valley in the area of the Chuya confluence, sometime from 18 to 38 ka ago, a landslide-dammed lake could have existed, the catastrophic drainage of which could have led to a significant movement of water masses and associated sediments (Deev et al., 2019).

For the Kurai Basin mega ripples, two clasts have provided burial ages of mid-to-late Holocene age. It is unlikely that these burial ages reflect the formation of the mega-ripples, because there is no evidence that large glacial-dammed and other lake basins were present during this period. Instead, the bleaching of clasts and their subsequent burial need to be explained by other, more recent, processes. First, this could be due to permafrost heaving. The thickness of the permafrost in the region of the Kurai and neighbouring Chuya depressions ranges from 6 to 100 m and more, and it has both a continuous and island distribution (Olenchenko et al., 2011). On the surface, it is manifested in the form of patterned ground and pingos. Thermokarst lakes are also associated with the degradation of permafrost. However, permafrost-associated sedimentological and landform phenomena are not known within our area. An alternative explanation is the overturning of boulders as a result of seismic shock and ground vibrations. This interpretation is supported by the consistency of our ages with the ages of palaeoearthquakes identified along the northern foot of the Kurai Range, which bounds the Kurai Basin from the north (Fig. 1a). At that location, surface ruptures with ^{14}C ages 5.8, 4.9, and 3.2 ka with Mw = 6.9–7.3 have been determined along the Kurai Fault Zone (Deev et al., 2017, 2021; Deev, 2019; Turova et al., 2020).

6. Conclusions

Rock-surface burial dating has shown promise for application in these mountainous areas, in particular, in the dating of the fluvial terraces of mountain rivers and intermontane depressions within the Russian Altai. Two age clusters were obtained (taking into account the dating uncertainty), of 16.7–21.4 ka and 2.2–6.4 ka. We associate the first cluster with a large-scale flood that occurred in the Katun valley as a result of deglaciation or the drainage of a landslide-dammed lake; the second is explained by local reworking events, perhaps associated with permafrost action or large palaeoearthquakes. Which of the two is the determining factor can only be shown by additional studies. However, to date, the good agreement of our ages with the ages of paleo-earthquakes, as well as the absence of signs of permafrost processes within the sampling site, leads us to favour the hypothesis of association with paleo-earthquakes.

Declaration of competing interest

The authors declare that they have no known competing financial interests or personal relationships that could have appeared to influence the work reported in this paper.

Acknowledgements

Luminescence dating was carried out as part of project № 19-17-00179 “Glacial history and catastrophic processes in Russian Altai in the Late Pleistocene – Holocene”, paleoseismologic research was supported by project № 21-17-0058 “Quaternary seismicity of the northern Altai Orogen: Evidence from paleoseismology, archaeoseismology, geophysics, geochronology, mineralogy, petrography, and isotope geochemistry”. ACC received funding from the Danish Council for Independent Research; AVP was supported by program № 0148-2019-0005 and RNK was supported by program № 121051100135-0.

References

Agatova, A.R., Nepop, R.K., Carling, P.A., Bohorquez, P., Khazin, L.B., Zhdanova, A.N., Moska, P., 2020. Last ice-dammed lake in the Kuray basin, Russian Altai: new results from multidisciplinary research. Earth Sci. Rev. 205, 103183 https://doi.org/10.1016/j.earscirev.2020.103183.

Ageby, L., Angelucci, D.E., Brill, D., Carrer, F., Rades, E.F., Rethemeyer, J., Brückner, H., Klasen, N., 2021. Rock surface IRSL dating of buried cobbles from an alpine dry-stone structure in Val di Sole, Italy. Quat. Geochronol. 66, 101212 https://doi.org/10.1016/j.quageo.2021.101212.

Aitken, M.J., 1985. Thermoluminescence Dating. Academic Press, London.

Baker, V.R., Benito, G., Rudoy, A.N., 1993. Palaeohydrology of late Pleistocene superflooding, altay mountains, Siberia. Science 259, 348–352. https://doi.org/10.1126/science.259.5093.348.

Baryshnikov, G.Ya, 1979. On the formation of large-boulder alluvium of the Biya river. In: Geol. And Mineral Resources of the Altai Territory: Abstracts of the Scientific and Practical Conf, pp. 117–119 (In Russian).

Butvilovsky, V.V., 1982. About traces of catastrophic discharges of glacial-dammed lakes in Eastern Altai. Evolution of river systems of the Altai Territory and questions of practice. In: Abstracts of the Scientific and Practical Conf, pp. 12–16 (In Russian).

Butvilovsky, V.V., 1993. Palaeogeography of the Last Glaciation and the Holocene of Altai: A Catastrophic Events Model. Tomsk University Press, Tomsk (In Russian).

Buylaert, J.P., Murray, A.S., Thomsen, K.J., Jain, M., 2009. Testing the potential of an elevated temperature IRSL signal from K-feldspar. Radiat. Meas. 44, 560–565. https://doi.org/10.1016/j.radmeas.2009.02.007.

Carling, P.A., 2013. Freshwater megaflood sedimentation: what can we learn about generic processes? Earth Sci. Rev. 125, 87–113. https://doi.org/10.1016/j.earscirev.2013.06.002.

Carling, P.A., Kirkbride, A.D., Parnachev, S., Borodavko, P.S., Berger, G.W., 2002. Late Quaternary catastrophic flooding in the Altai Mountains of south–central Siberia: a synoptic overview and introduction to flood deposit sedimentology. In: Martini, I.P., Baker, V.R., Garzón, G. (Eds.), Flood and Megaflood Processes and Deposits: Recent and Ancient Examples. International Association of Sedimentologists. Blackwell Science, Oxford, pp. 17–35. https://doi.org/10.1002/9781444304299.ch2.

Cresswell, A.J., Carter, J., Sanderson, D.C.W., 2018. Dose rate conversion parameters: assessment of nuclear data. Radiat. Meas. 120, 195–201. https://doi.org/10.1016/j.radmeas.2018.02.007.

Cunningham, A.C., Buylaert, J.-P., Murray, A.S., 2021. Beta attenuation in granular matrices: implications for trapped-charge dating. Geochronology. https://doi.org/10.5194/gchron-2021-17 (Preprint).

Cunningham, A.C., Khashchevskaya, D., Semikolennykh, D., Kurbanov, R., Murray, A.S., 2022. Luminescence dating of mass-transport sediment using rock-surface burial methods: a test case from the Baksan valley in the Caucasus Mountains. Quat. Geochronol. 68, 101253 https://doi.org/10.1016/j.quageo.2022.101253.

Deev, E.V., 2019. Localization zones of ancient and historical earthquakes in Gorny Altai. Izvestiya Phys. Solid Earth 55 (3), 451–470. https://doi.org/10.31857/S0002-33372019371-96 (In Russian).

Deev, E.V., Gibsher, A.S., Chigvintseva, L.A., Frolova, T.V., Ryabinin, A.B., 2005. Seismites in Pleistocene sediments of gornyi Altai. Dokl. Earth Sci. 403, 681–686.

Deev, E.V., Zolnikov, I.D., Gus'kov, S.A., 2009. Seismites in quaternary sediments of southeastern Altai. Russ. Geol. Geophys. 50, 546–561. https://doi.org/10.1016/j.rgg.2008.10.004.

Deev, E.V., Zolnikov, I.D., Bortodovsky, A.P., Goltsova, S.V., 2012. Neotectonics and palaeoseismicity of the lower Katun' valley (gorny Altai). Russ. Geol. Geophys. 53, 883–894. https://doi.org/10.1016/j.rgg.2012.07.004.

Deev, E.V., Zolnikov, I.D., Goltsova, S.V., Rusanov, G.G., Emanov, A.A., 2013. Traces of palaeoearthquakes in the Quaternary deposits of intermontane basins in central Gorny Altai. Russ. Geol. Geophys. 54, 312–323. https://doi.org/10.1016/j.rgg.2013.02.006.

Deev, E.V., Zolnikov, I.D., Lobova, E.Yu, 2015. Late pleistocenee–holocene coseismic deformations in the malyi yaloman River Valley (gorny Altai). Russ. Geol. Geophys. 56, 1256–1272. https://doi.org/10.1016/j.rgg.2015.08.003.

Deev, E.V., Turova, I.V., Borodovskiy, A.P., Zolnikov, I.D., Oleszczak, L., 2017. Unknown large ancient earthquakes along the Kurai fault zone (Gorny Altai): new results of palaeoseismological and archaeoseismological studies. Int. Geol. Rev. 59 (3), 293–310. https://doi.org/10.1080/00206814.2016.1258675.

Deev, E.V., Zolnikov, I.D., Turova, I.V., Rusanov, G.G., Ryapolova, Y.M., Nevedrova, N.N., Kotler, S.A., 2018. Palaeoearthquakes in the Uimon Basin (gorny Altai). Russ. Geol. Geophys. 59, 351–362. https://doi.org/10.1016/j.rgg.2017.07.011.

Deev, E., Turova, I., Borodovskiy, A., Zolnikov, I., Pozdnyakova, N., Molodkov, A., 2019. Large earthquakes in the Katun fault Zone (gorny Altai): palaeoseismological and archaeoseismological evidence. Quat. Sci. Rev. 203, 68–89. https://doi.org/10.1016/j.quascirev.2018.11.009.

Deev, E.V., Dublyansky, Y.V., Pozdnyakova, N.I., Scholz, D., Kokh, S.N., Sokol, E.V., Rusanov, G.G., 2021. 230Th/U dating of travertines related to palaeoearthquakes in Gorny Altai: first results. Dokl. Earth Sci. 500 (2), 820–825.

Deev, E.V., Zolnikov, I.D., Kurbanov, R.N., Panin, A.V., Murray, A., Korzhenkov, A.M., Turova, I.V., Pozdnyakova, N.I., Vasiliev, A.V., 2022. OSL age of the Sukor landslide: significance for palaeoseismology and palaeogeography of Gorny Altai. Russ. Geol. Geophys. (in press).

Freiesleben, T., Sohbati, R., Murray, A.S., Jain, M., al Khasawneh, S., Hvidt, S., Jakobsen, B., 2015. Mathematical model quantifies multiple daylight exposure and burial events for rock surfaces using luminescence dating. Radiat. Meas. 81, 16–22. https://doi.org/10.1016/j.radmeas.2015.02.004.

Gribenski, N., Jansson, K.N., Lukas, S., Stroeven, A.P., Harbor, J.M., Blomdin, R., Ivanov, M.N., Heyman, J., Petrakov, D.A., Rudoy, A., Clifton, T., Lifton, N.A., Caffee, M.W., 2016. Complex patterns of glacier advances during the late glacial in the Chagan Uzun Valley, Russian Altai. Quat. Sci. Rev. 149, 288–305. https://doi.org/10.1016/j.quascirev.2016.07.032.

Herget, J., 2005. Reconstruction of Ice-Dammed Lake Outburst Floods in the Altai Mountains, Siberia. GSA, Boulder. https://doi.org/10.1130/0-8137-2386-8.1.

Herget, J., Agatova, A.R., Carling, P.A., Nepop, R.K., 2020. Altai megafloods – the temporal context. Earth Sci. Rev. 200, 1–22. https://doi.org/10.1016/j.earscirev.2019.102995, 102995.

Jenkins, G.T., Duller, G.A.T., Roberts, H.M., Chiverrell, R.C., Glasser, N.F., 2018. A new approach for luminescence dating glaciofluvial deposits – high precision optical dating of cobbles. Quat. Sci. Rev. 192, 263–273. https://doi.org/10.1016/j.quascirev.2018.05.036.

Kreutzer, S., Dietze, M., 2021. plot_GrowthCurve( ): fit and plot a growth curve for luminescence data (Lx/Tx against dose). Function version 1.11.4. In: Kreutzer, S., Burow, C., Dietze, M., Fuchs, M.C., Schmidt, C., Fischer, M., Friedrich, J., Mercier, N., Philippe, A., Riedesel, S., Autzen, M., Mittelstrass, D., Gray, H.J., Galharret, J. (Eds.), Luminescence: Comprehensive Luminescence Dating Data Analysis. R package version 0.9.16. https://CRAN.R-project.org/package=Luminescence.

Lehmkuhl, F., Zander, A., Frechen, M., 2007. Luminescence chronology of fluvial and aeolian deposits in the Russian Altai (Southern Siberia). Quat. Geochronol. 2, 195–201. https://doi.org/10.1016/j.quageo.2006.04.005.

Murray, A., Wintle, A., 2000. Luminescence dating of quartz using an improved single-aliquot regenerative-dose protocol. Radiat. Meas. 32 (1), 57–73. https://doi.org/10.1016/S1350-4487(99)00253-X.

Murray, A.S., Wintle, A.G., 2003. The single aliquot regenerative dose protocol: potential for improvements in reliability. Radiat. Meas. 37, 377–381. https://doi.org/10.1016/S1350-4487(03)00053-2.

Murray, A., Marten, R., Johnston, A., Martin, P., 1987. Analysis for naturally occurring radionuclides at environmental concentrations by gamma spectrometry. J. Radioanal. Nucl. Chem. 115, 263–288.

Murray, A.S., Helsted, L.M., Jain, M., Buylaert, J.-P., 2018. Measurement of natural radioactivity: calibration and performance of a high-resolution gamma spectrometry facility. Radiat. Meas. 120, 215–220. https://doi.org/10.1016/j.radmeas.2018.04.006.

Olenchenko, V.V., Kozhevnikov, N.O., Antonov, E.Yu, Pospeeva, E.V., Potapov, V.V., Shein, A.N., Stefanenko, S.M., 2011. Distribution of permafrost in Chuiskaya Basin (Gorny Altai) according to transient electromagnetic soundings data. Earths Cryosphere 15 (1), 15–22 (In Russian).

Panin, A., Baryshnikov, G., 2015b. Old valley of Chuya – its age and mechanism of abandonment. In: Baryshnikov, G., Agatova, A., Carling, P., Herget, J., Panin, A., Adamiec, G., Nepop, R. (Eds.), Russian Altai in the Last Pleistocene and the Holocene – Geomorphological Catastrophes and Landscape Rebound (Fieldtrip Guide). ASU Publ., Barnaul, pp. 115–119.

Panin, A., Adamiec, G., Baryshnikov, G., 2015a. General description and absolute geochronology of the Bolshoi Yaloman exposure. In: Baryshnikov, G., Agatova, A., Carling, P., Herget, J., Panin, A., Adamiec, G., Nepop, R. (Eds.), Russian Altai in: the Last Pleistocene and the Holocene – Geomorphological Catastrophes and Landscape Rebound (Fieldtrip Guide). ASU Publ., Barnaul, pp. 41–47.

Panin, A., Baryshnikov, G., Adamiec, G., 2015c. Kuray strandlines – supplement. In: Baryshnikov, G., Agatova, A., Carling, P., Herget, J., Panin, A., Adamiec, G., Nepop, R. (Eds.), Russian Altai in the Last Pleistocene and the Holocene – Geomorphological Catastrophes and Landscape Rebound (Fieldtrip Guide). ASU Publ., Barnaul, pp. 106–107.

Panin, A.V., Baryshnikov, G.Ya, Deev, E.V., Zolnikov, I.D., Kurbanov, R.N., 2021. Geomorphological and sedimentological data to refining the chronology of the Altai megafloods. In: 2021. Materials of the II All-Russian Scientific Conference Dedicated to the Memory of Professor A.A. Velichko (Moscow, November 22-25, 2021), pp. 75–78 (In Russian).

Prescott, J.R., Hutton, J.T., 1994. Cosmic ray contributions to dose rates for luminescence and ESR dating: large depths and long-term variations. Radiat. Meas. 23, 497–500. https://doi.org/10.1016/1350-4487(94)90086-8.

Rades, E., Sohbati, R., Lüthgens, C., Jain, M., Murray, A., 2018. First luminescence- depth profiles from boulders from moraine deposits: insights into glaciation chronology and transport dynamics in Malta valley, Austria. Radiat. Meas. 120, 281–289. https://doi.org/10.1016/j.radmeas.2018.08.011.

Reuther, A., Herget, J., Ivy-Ochs, S., Borodavko, P., Kubik, P.W., Heine, K., 2006. Constraining the timing of the most recent cataclysmic flood event from ice-dammed lakes in the Russian Altay Mountains, Siberia, using cosmogenic in-situ 10Be. Geology 34, 913–916. https://doi.org/10.1130/G22755A.1.

Riedesel, S., Autzen, M., 2020. Beta and gamma dose rate attenuation in rocks and sediment. Radiat. Meas. 133, 106295 https://doi.org/10.1016/j.radmeas.2020.106295.

Rudoy, A.N., 1984. Giant ripples of the current – proof of catastrophic outbursts of glacial lakes in Altai. In: Modern geomorphological processes in the Altai Territory, pp. 60–64 (In Russian).

Rudoy, A.N., 1995. Geomorphological effect and hydraulics of the Late Pleistocene jökulhlaups of the ice-dammed lakes in Altai. Russ. Geomorphol. 4, 61–76 (In Russian).

Sohbati, R., Murray, A., Jain, M., Buylaert, J.-P., Thomsen, K., 2011. Investigating the resetting of OSL signals in rock surfaces. Geochronometria 38 (3), 249–258. https://doi.org/10.2478/s13386-011-0029-2.

Sohbati, R., Murray, A.S., Buylaert, J.-P., Almeida, N.A.C., Cunha, P.P., 2012. Optically stimulated luminescence (OSL) dating of quartzite cobbles from the Tapada do Montinho archaeological site (east-central Portugal). Boreas 41 (3), 452–462. https://doi.org/10.1111/j.1502-3885.2012.00249.x.

Sohbati, R., Murray, A., Porat, N., Jain, M., Avner, U., 2015. Age of a prehistoric "Rodedian" cult site constrained by sediment and rock surface luminescence dating techniques. Quat. Geochronol. 30, 90–99. https://doi.org/10.1016/j.quageo.2015.09.002.

Souza, P.E., Sohbati, R., Murray, A.S., Kroon, A., Clemmensen, L.B., Hede, M.U., Nielsen, L., 2019. Luminescence dating of buried cobble surfaces from sandy beach ridges: a case study from Denmark. Boreas 48, 841–855. https://doi.org/10.1111/bor.12402.

Thomsen, K.J., Murray, A.S., Jain, M., Bøtter-Jensen, L., 2008. Laboratory fading rates of various luminescence signals from feldspar-rich sediment extracts. Radiat. Meas. 43, 1474–1486. https://doi.org/10.1016/j.radmeas.2008.06.002.

Turova, I., Deev, E., Pozdnyakova, N., Entin, A., Nevedrova, N., Shaparenko, I., Bricheva, S., Korzhenkov, A., Kurbanov, R., Panin, A., 2020. Surface-rupturing palaeoearthquakes in the Kurai Fault zone (gorny Altai, Russia): trenching and geophysical evidence. J. Asian Earth Sci. 197, 104399 https://doi.org/10.1016/j.jseaes.2020.104399.

Wallinga, J., Murray, A.S., Wintle, A.G., 2000. Single-aliquot regenerative-dose (SAR) protocol applied to coarse-grain feldspar. Radiat. Meas. 32, 529–533. https://doi.org/10.1016/S1350-4487(00)00091-3.

Zolnikov, I.D., 2008. Stratotypes of quaternary deposits of the yaloman-katun' zone (gorny Altai). Russ. Geol. Geophys. 49, 682–691. https://doi.org/10.1016/j.rgg.2007.09.021.

Zolnikov, I.D., Deev, E.V., 2013. Quaternary glacial superfloods at the Gorny Altai: formation conditions and geological features. Earths Cryosphere 17, 74–82 (In Russian).

Zolnikov, I.D., Deev, E.V., Kotler, S.A., Rusanov, G.G., Nazarov, D.V., 2016. New results of OSL dating of Quaternary sediments in the Upper Katun' valley (Gorny Altai) and adjacent area. Russ. Geol. Geophys. 57 (6), 933–943. https://doi.org/10.1016/j.rgg.2015.09.022.

Zolnikov, I.D., Deev, E.V., Kurbanov, R.N., Panin, A.V., Vasiliev, A.V., Pozdnyakova, N.I., Turova, I.V., 2021. Age of the chibit glaciation in gornyi Altai. Dokl. Earth Sci. 496 (2), 176–181. https://doi.org/10.1134/S1028334X21020227.